JACS
JOURNAL OF THE AMERICAN CHEMICAL SOCIETY
Article
pubs.acs.org/JACS

Removal of Interstitial H_2O in Hexacyanometallates for a Superior Cathode of a Sodium-Ion Battery

Jie Song,[†] Long Wang,[§] Yuhao Lu,[§] Jue Liu,[∥] Bingkun Guo,[†] Penghao Xiao,[‡] Jong-Jan Lee,[§] Xiao-Qing Yang,[⊥] Graeme Henkelman,[‡] and John B. Goodenough*,[†]

[†]Materials Science and Engineering Program and Texas Materials Institute and [‡]Department of Chemistry and the Institute for Computational and Engineering Sciences, The University of Texas at Austin, Austin, Texas 78712, United States

[§]Sharp Laboratories of America, Camas, Washington 98607, United States

[∥]Department of Chemistry, State University of New York at Stony Brook, Stony Brook, New York 11794, United States

[⊥]Department of Chemistry, Brookhaven National Laboratory, Upton, New York 11973, United States

Supporting Information

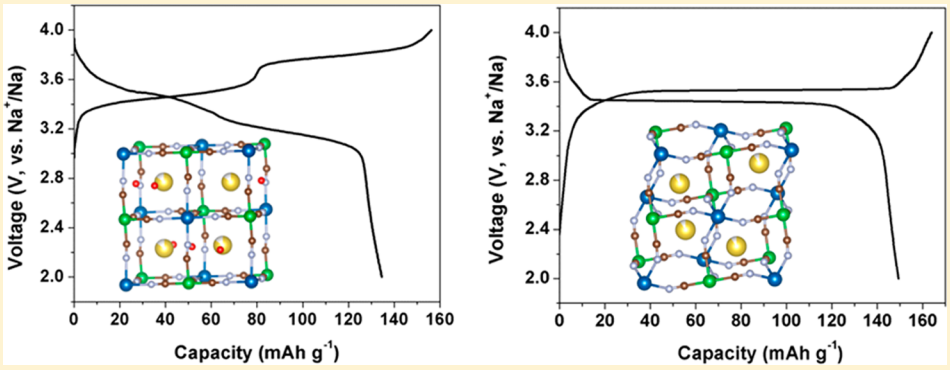

ABSTRACT: Sodium is globally available, which makes a sodium-ion rechargeable battery preferable to a lithium-ion battery for large-scale storage of electrical energy, provided a host cathode for Na can be found that provides the necessary capacity, voltage, and cycle life at the prescribed charge/discharge rate. Low-cost hexacyanometallates are promising cathodes because of their ease of synthesis and rigid open framework that enables fast Na^+ insertion and extraction. Here we report an intriguing effect of interstitial H_2O on the structure and electrochemical properties of sodium manganese(II) hexacyanoferrates(II) with the nominal composition $Na_2MnFe(CN)_6{\cdot}zH_2O$ ($Na_{2-\delta}MnHFC$). The newly discovered dehydrated $Na_{2-\delta}MnHFC$ phase exhibits superior electrochemical performance compared to other reported Na-ion cathode materials; it delivers at 3.5 V a reversible capacity of 150 mAh g^{-1} in a sodium half cell and 140 mAh g^{-1} in a full cell with a hard-carbon anode. At a charge/discharge rate of 20 C, the half-cell capacity is 120 mAh g^{-1}, and at 0.7 C, the cell exhibits 75% capacity retention after 500 cycles.

INTRODUCTION

Large-capacity, cost-effective electrical-energy storage is the transformational technology needed to enable large-scale integration of renewable energy into the grid and to increase dramatically power generation and transmission efficiency.[1] To date, pumped-hydro and compressed-air energy storage are widely used, but both have serious infrastructure requirements that limit large-scale energy storage to specific sites. Rechargeable, low-cost batteries would provide distributed electrical-energy storage. Lithium-ion batteries (LiIBs) are the leading option for this application, but the use of lithium is hampered by cost and supply restriction. Therefore, a room-temperature sodium-ion battery (NaIB) for large-scale storage of electrical energy is an attractive technical target.[2−4]

Recently, hexacyanometallates $A_xM_1[M_2(CN)_6]_y{\cdot}z\,H_2O$ (A = alkaline metal; M_1 and M_2 = transition metal ions; $0 \le x \le 2$; $y \le 1$) have been investigated as NaIB cathodes in both aqueous[5−8] and nonaqueous electrolytes,[9−14] owing to their ease of synthesis and rigid open framework with large interstitial space. The structure of $A_xM_1[M_2(CN)_6]_y{\cdot}zH_2O$, with $y = 1$, consists of a double perovskite framework with $(C{\equiv}N)^-$ anions bridging M_1N_6 and M_2C_6 octahedra; A^+ and H_2O occupy the large space of the framework's interstitial sites. The interstitial water forms $(AOH_2)^+$ molecules that H-bond to the framework.[15,16] The operational voltage with an aqueous electrolyte is restricted to the 1.5 V range, so the Na_xM_1 HCF framework Na-ion cathodes in a nonaqueous electrolytes is an alternative way to increase the energy density of NaIBs. The most promising candidate among these Na_xM_1HCF Na-ion

Received: December 4, 2014
Revised: January 28, 2015
Accepted: January 29, 2015
Published: February 13, 2015

DOI: 10.1021/ja512383b
J. Am. Chem. Soc. 2015, 137, 2658−2664

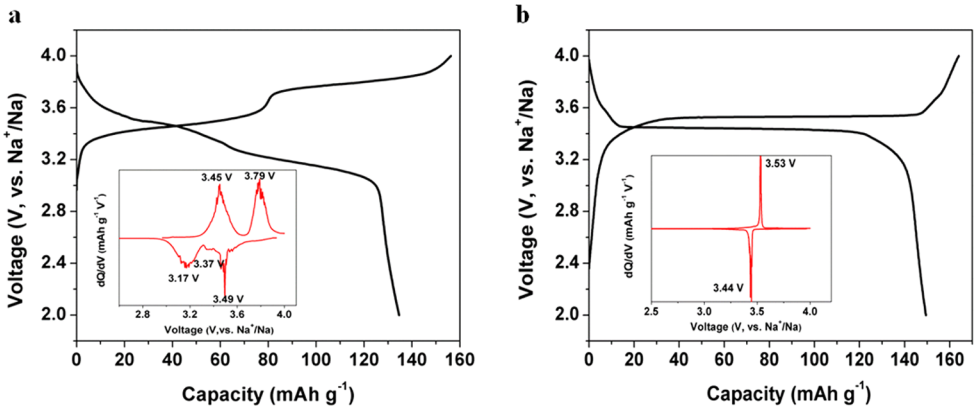

Figure 1. Galvanostatic initial charge and discharge profiles of (a) air-dried and (b) vacuum-dried $Na_{2-\delta}MnHCF$ at a current of 0.1 C (15 mA g^{-1}) in the voltage range of 2.0−4.0 V. The derivative curves (dQ/dV) plotted as a function of V are shown as inserts.

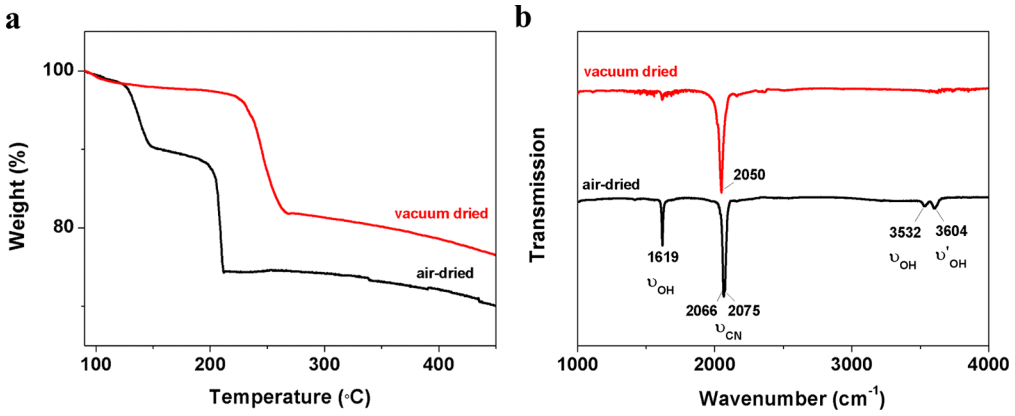

Figure 2. (a) TGA curves and (b) IR spectra of air-dried and vacuum-dried $Na_{2-\delta}MnHCF$. The TGA test was conducted at a heating rate of 5 °C min^{-1} under N_2 flow.

cathodes is the discharged nominal $Na_2Mn[Fe(CN)_6]\cdot zH_2O$, which contains only earth-abundant elements and enables two Na^+ per formula unit to cycle reversibly. Although Imanishi et al.[17] explored the affect of the number of coordinating water molecules on Li^+ intercalation in $Fe_4[Fe(CN)_6]_3\cdot zH_2O$, the details of the correlation among interstitial water within hexacyanometallates and their crystalline structures and electrochemical properties have remained unknown. In this paper, we carefully investigated the role of interstitial H_2O in determining the structural and electrochemical properties of $Na_{2-\delta}MnHFC$. Removal of interstitial H_2O leads to the discovery of a new dehydrated $Na_{2-\delta}MnHFC$ phase that exhibits different electrochemical behavior than the hydrated phase and shows a high reversible capacity at 3.5 V with excellent rate and cycling performance.

RESULTS AND DISCUSSION

The as-prepared $Na_{2-\delta}MnHCF$ precipitate was separated into two parts; both parts were dried at 100 °C, one under air and the other under vacuum. Figure 1 compares the first-cycle charge/discharge curves of air-dried and vacuum-dried samples in sodium half cells. The air-dried $Na_{2-\delta}MnHFC$ electrode exhibits two steps, at 3.45 and 3.79 V on charge and at 3.17 and 3.49 V on discharge. In contrast, vacuum-dried $Na_{2-\delta}MnHCF$ exhibits an apparently single flat plateau at 3.53 V on charge, at 3.44 V on discharge with a higher cycle efficiency, at 100 versus 300 mV between charge and discharge, and a higher reversible capacity (150 mAh g^{-1}) at a rate of 0.1 C over the range of $2.0 \leq V \leq 4.0$ V.

Both white powder samples have the same noncubic shape with a particle size of 200−400 nm (Figure S1) and the same molar Na/Fe/Mn ratio of 1.89:0.97:1.00 as determined by inductively coupled plasma (ICP) analysis. Thermogravimetric analysis (TGA) of the air-dried sample shows three distinct weight-loss events (Figure 2a): a first step occurring below 120 °C corresponds to the loss of adsorbed water, the second step occuring in the range of $120 < T < 190$ °C can be assigned to the elimination of interstitial water,[16,18] and the sharp weight loss occurring near 190 °C indicates the decomposition of the MnHCF framework. The weight loss over the second step corresponds to $z = 1.87$. TGA of the vacuum-dried sample shows little weight loss in the interval $120 < T < 225$ °C and a sharp loss in the range $225 < T < 275$ °C; its total water content is considered to be $z = 0.3$. The infrared (IR) spectra in Figure 2b also suggest the removal of interstitial water by vacuum-drying. Sharp absorptions at 1619 and 3532 cm^{-1} in the IR spectra of air-dried $Na_{2-\delta}MnHCF$ are associated with the O−H stretching and H−O−H bending modes arising from interstitial water, and the peak at 3604 cm^{-1} is characteristic of free surface water (nonhydrogen bonded).[19,20]

The Synchroton X-ray diffraction (SXRD) data (Figure 3a,c) of the two powders were first indexed and then refined by the Rietveld method in Topas software (version 4.2). Although attempts to determine the locations of H atoms in the hydrated sample were unsuccessful, a reasonable structure with an

DOI: 10.1021/ja512383b
J. Am. Chem. Soc. 2015, 137, 2658−2664

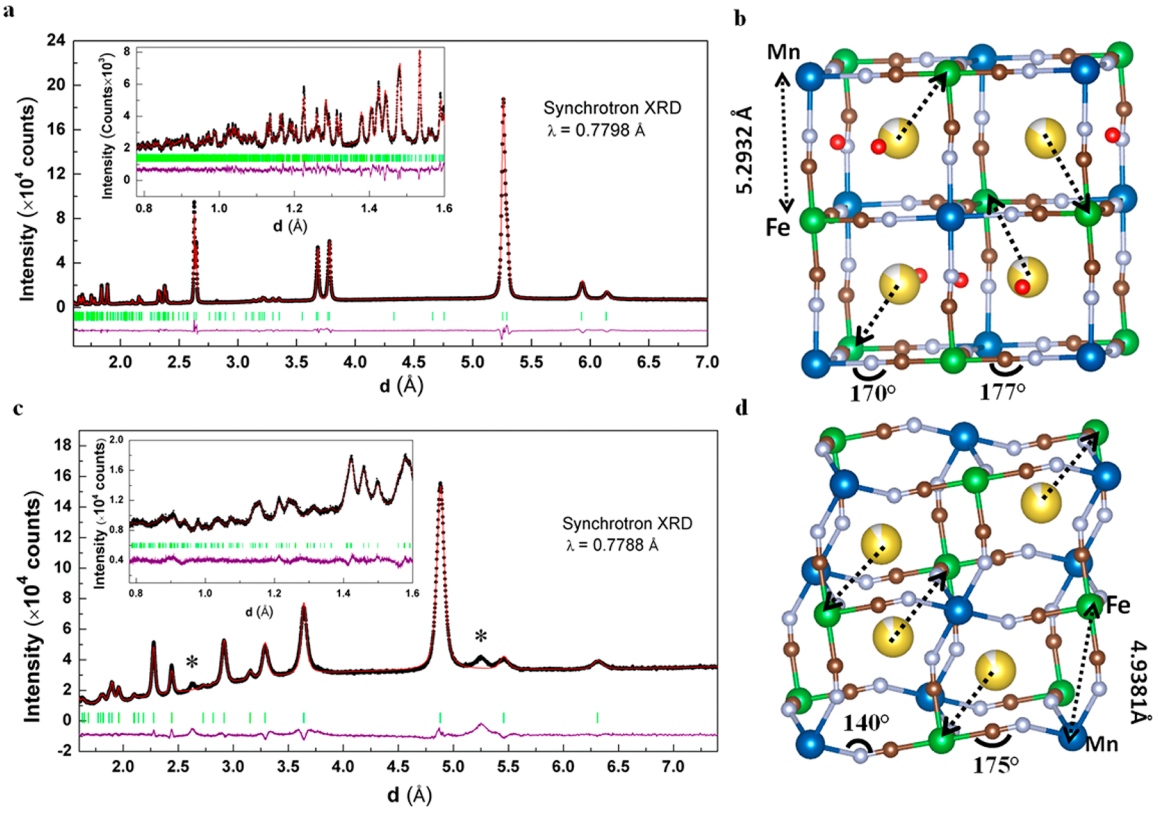

Figure 3. Synchroton X-ray diffraction (SXRD) patterns of (a) M-$Na_{2-\delta}$MnHCF and (c) R-$Na_{2-\delta}$MnHCF. Local structures of (b) M-$Na_{2-\delta}$MnHCF and (d) R-$Na_{2-\delta}$MnHCF, showing the Na^+ displacements and distorted framework. In a and c, the black dots show observed data, the red lines are the calculated patterns, the purple lines correspond to the difference between the observed and calculated patterns, and the vertical green bars are the expected positions of Bragg reflections. Asterisks in c show peaks from absorbed water during the sample preparation for SXRD. In-house XRD pattern (Figure S2a) shows a single rhombohedral $Na_{2-\delta}$MnHCF phase. In b and d, high-spin Mn^{II} is blue, low-spin Fe^{II} is green, N is silver, C is dark brown, Na is yellow, and O is red.

oxygen position (in H_2O) has been obtained by Rietveld refinement, with atomic positions shown in Table S1a. The atomic positions in the dehydrated sample were identified by SXRD and time-of-flight (TOF) neutron diffraction (Figure S2 and Table S1b). The hydrated $Na_{2-\delta}$MnHCF structure is monoclinic (space group = $P2_1/n$, a = 10.5864, b = 7.5325, c = 7.3406 Å, and β = 92.119°); the dehydrated $Na_{2-\delta}$MnHCF structure is rhombohedral (space group = $R\bar{3}$, $a = b$ = 6.5800, c = 18.9293 Å). Their local structures are also illustrated in Figure 3b,d.

The monoclinic M-$Na_{2-\delta}$MnHFC and rhombohedral R-$Na_{2-\delta}$MnHCF samples have the same composition except for the water content, which shows that the interstitial H_2O plays a key role in the structures as well as on the electrochemical voltage profile of nominal $Na_{2-\delta}MnFe(CN)_6{\cdot}zH_2O$. In the dehydrated rhombohedral phase, the Na^+ are cooperatively displaced along a cubic [111] axis toward the Fe vertex, and a cooperative rotation of the linear $(C{\equiv}N)^-$ anions brings the N atoms toward the displacement axis to make contact with the displaced Na^+ ions. Incorporation of interstitial water transforms the rhombohedral structure to a monoclinic one. The monoclinic distortion reflects a cooperative distortion of $(NaOH_2)^+$ groups, with the Na^+ displaced along alternating cubic [111] and [1−11] axes and the Na moving toward the Fe vertices in neighboring (010) planes with the oxygen atoms displaced to near a face bridging neighboring Na atoms. Although the strong C≡N bond keeps these anions linear, they are cooperatively rotated from the cubic Mn−N≡C−Fe axis. The rhombohedral structure has a smaller volume and a larger distortion from the cubic symmetry than does the monoclinic phase (Figure 3b,d). The shorter Mn···Fe distance in R-$Na_{2-\delta}$MnHCF is due to a larger rotation of the $(C{\equiv}N)^-$ anion from the Mn−N≡C−Fe bond axis, which reduces the Mn···Fe separation and lowers the volume. Moreover, the energies of the HS Mn^{III}/Mn^{II} and LS Fe^{III}/Fe^{II} couples are controlled by σ-bonding Mn−N and π-bonding Fe−C interactions, respectively, so that they respond differently to the degree of the rotation of the linear $(C{\equiv}N)^-$ anions from the Mn···Fe axes. This difference can account for the merger of the two voltage plateaus in the hydrated sample to essentially one plateau in the dehydrated sample.

Ex situ XRD measurements show that different structural changes occur during the Na^+ deinsertion/insertion process for M-$Na_{2-\delta}$MnHCF and R-$Na_{2-\delta}$MnHCF samples. On Na^+ extraction from M-$Na_{2-\delta}$MnHCF, the XRD spectrum shows a merger of doublets into sharp single peaks and the disappearance of a peak at 14.9°, indicating a phase transformation from a monoclinic phase to a cubic one over the first voltage plateau (Figure 4a); apparently, the $(NaOH_2)^+$ and Na^+ displacements become disordered at room temperature with the removal of one Na^+ per formula unit. The XRD pattern with all Na^+ removed was indexed with tetragonal symmetry ($a = b$ =10.1186 Å and c = 10.5414 Å), consistent with a cooperative Jahn−Teller distortion of the $Mn^{III}N_6$ octahedra (Figure 4b). The cubic unit cell expands with one Na^+ per formula unit; the volume of the M phase with all Na^+

DOI: 10.1021/ja512383b
J. Am. Chem. Soc. 2015, 137, 2658−2664

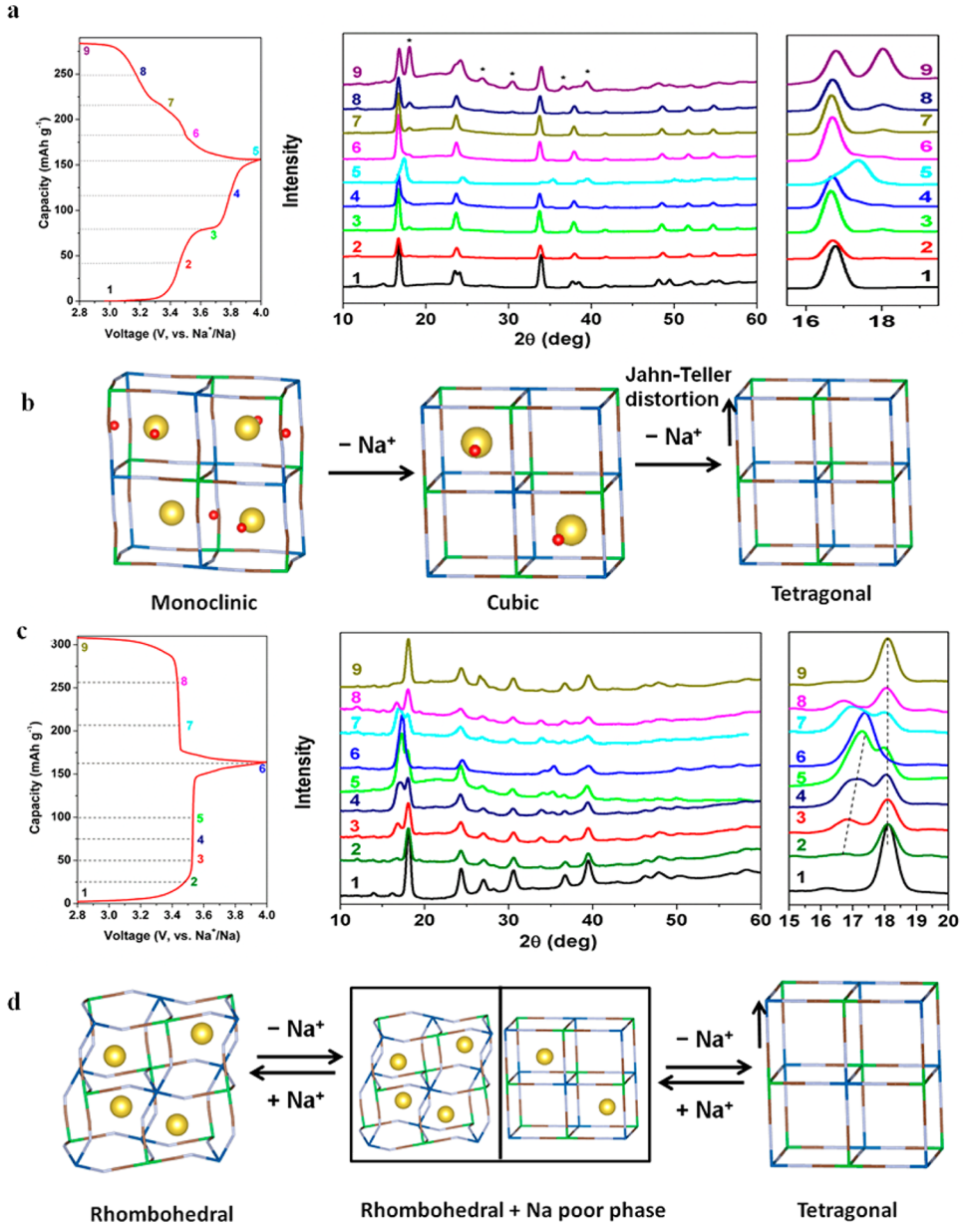

Figure 4. Ex situ XRD patterns of (a) M-$Na_{2-\delta}$MnHCF and (c) R-$Na_{2-\delta}$MnHCF at different states at the first cycle. Schematic illustration of structural evolution of (b) M-$Na_{2-\delta}$MnHCF and (d) R-$Na_{2-\delta}$MnHCF along with Na^+ extraction and insertion.

removed is smallest (Figure S3). On return of two Na^+ per formula unit, the single monoclinic phase was not returned; instead, a mixture of the M and R phases was found, indicating a segregation into dehydrated and hydrated phases. A segregation of the water content apparently takes place on the initial removal of Na^+ ions because a small shoulder from the rhombohedral phase already appears in the XRD pattern when the electrode is charged to 3.46 V at the first cycle. On removal of Na from the dehydrated R phase, the intensity of the R-phase peaks systematically decrease at the expense of a second Na-poor phase with a larger volume that evolves to a tetragonal phase as all Na^+ is extracted (Figure 4c,d). On the return of two Na^+ ions per formula unit, the XRD evolution is reversed to a well-developed R-phase XRD pattern.

The phase transition between M and R is reversible: for $\delta \approx 0$, thermal removal of interstitial H_2O from the hydrated phase induces the M to R structural change and exposure of the R phase to air with 80% humidity for 20 h at room temperature transforms the R phase to the M phase (Figure S4). In addition, a hydrated M phase showed the onset of a new voltage plateau after the first charge/discharge cycle at around 3.4 V that grew in capacity with increased cycling with a complementary decrease in the capacities of the 3.45/3.17 and 3.79/3.49 V plateaus. After the 10th cycle, the 3.4 V plateau, characteristic of the R phase, contributes most of the capacity, as shown in Figure S5. Figure S6 shows the XRD spectrum of the M-$Na_{2-\delta}$MnHCF electrode after 20 cycles. The R phase is dominant with a smaller concentration of the M phase, which is consistent with the segregation into a dehydrated ($z = 0$) phase and a $z \approx 2$ phase that are caused by the loss of H_2O on cycling. Calculation[21] shows that the binding energy of H_2O in the lattice becomes much weaker if it is unattached to a Na^+ ion, dropping from 0.8 to less than 0.1 eV, supporting the

DOI: 10.1021/ja512383b
J. Am. Chem. Soc. 2015, 137, 2658–2664

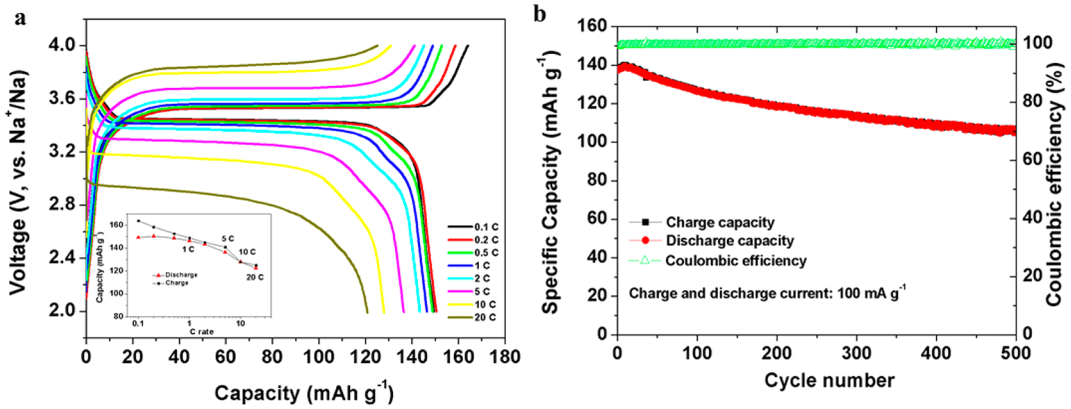

Figure 5. (a) Rate capability of a Na/R-$Na_{2-\delta}$MnHCF cell. (b) Capacity retention of R-$Na_{2-\delta}$MnHCF cells over 500 cycles.

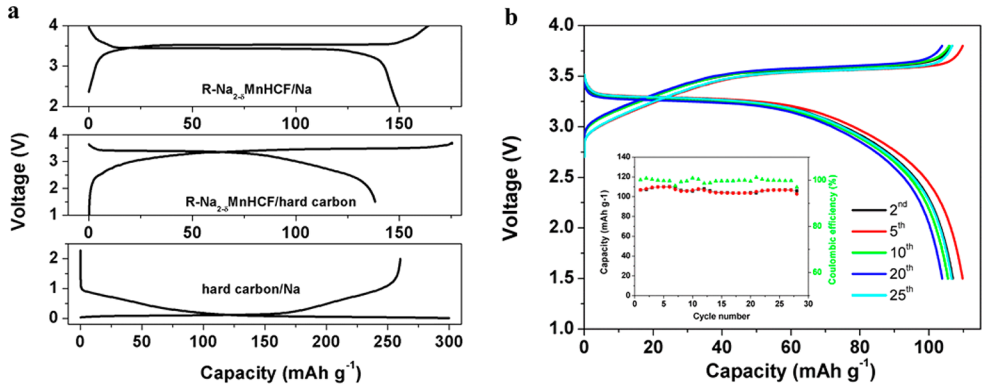

Figure 6. (a) The initial charge/discharge galvanostatic curves of the R-$Na_{2-\delta}$MnHCF/Na half cell, hard-carbon/R-$Na_{2-\delta}$MnHCF full cell and hard-carbon/Na half cell. (b) Charge and discharge curves of a hard-carbon/Na_xMnHCF full cell for the first 25 cycles. The full cell was cycled in the range of 3.8−1.5 V at a charge and discharge current of 100 mA g^{-1}. The inset of b shows the capacity retention and Coulombic efficiency during cycling. All the specific capacity and current density in full cells were normalized by the active mass of $Na_{2-\delta}$MnHCF.

conclusion that H_2O is extracted with Na^+ ions of a hydrated unit cell containing $(NaOH_2)^+$ units.

Figure 5a shows that R-$Na_{2-\delta}$MnHCF has an excellent rate capability in a sodium half cell for both charge and discharge, retaining 81% of its capacity when the discharge rate increases from 0.1 to 20 C. At 0.7 C, R-$Na_{2-\delta}$MnHCF retained 75% capacity after 500 cycles with a high Coulombic efficiency of nearly 100% (Figure 5b). The 150 mAh g^{-1} reversible capacity of R-$Na_{2-\delta}$MnHCF with a flat 3.5 V versus Na^+/Na is comparable to that of $LiFePO_4$ in a Li-ion battery; R-$Na_{2-\delta}$MnHCF gives a performance superior, in terms of reversible capacity, rate capability, and cyclability, to that of the cathode materials for a reversible Na-ion battery that have been reported in the literature (Table S2). However, to date, metallic sodium is not a practical anode for a rechargeable Na-ion battery. Therefore, rechargeable Na-ion batteries are fabricated in a discharged state with an insertion-compound host or metal that alloys reversibly with Na as the anode. We have chosen hard carbon as the anode for a full-cell test. On the basis of the mass of R-$Na_{2-\delta}$MnHCF, we obtained a reversible capacity of 140 mAh g^{-1} over the voltage range $1.5 \leq V \leq 3.8$ V in the full cell (Figure 6a). This full cell gave a moderate rate performance, with 96 mAh g^{-1} at 2 C, as shown in Figure S7. No obvious capacity fade was observed over 30 cycles at 100 mA g^{-1} (0.7 C) with a Coulombic efficiency nearly 100% (Figure 6b).

In summary, an intriguing effect of interstitial H_2O on the structure and electrochemical properties of $Na_{2-\delta}$MnHCF has been revealed. The removal of interstitial H_2O either thermally or electrochemically from the MnHCF framework induces a structural transition and a profound electrochemical property change. Dehydrated rhombohedral $Na_{2-\delta}$MnHCF delivers 150 mAh g^{-1} with flat charge and discharge plateaus at 3.5 V; it exhibits excellent rate capability and cycling performance. Full cells with hard carbon as the anode have also been demonstrated to have a 140 mAh g^{-1} reversible capacity at moderate charge/discharge rates. The dehydrated $Na_{2-\delta}$MnHCF cathode promises to be a competitive, low-cost cathode of rechargeable NaIBs for large-scale applications. Furthermore, understanding the critical effect of interstitial H_2O also provides an instructive insight for the development of other hexacyanometallates for alkali ion batteries.

■ MATERIALS AND METHODS

Materials Synthesis. Synthesis of $Na_{2-\delta}$MnHCF was carried out as described elsewhere in the literature,[11] with slight modification. Briefly, 3 mmol of $Na_4Fe(CN)_6$ and 14.0 g of NaCl were dissolved in a solution of 75 mL of distilled water and 25 mL of ethanol. A 100 mL solution containing 6 mmol of $MnCl_2{\cdot}4H_2O$ was slowly dropped into the $Na_4Fe(CN)_6$ solution under strong stirring. The obtained white precipitate of $Na_{2-\delta}$ MnHCF was washed with distilled water and was dried using two conditions: (1) 100 °C in air and (2) 100 °C in vacuum. Dehydration was achieved by evacuating MnHCF to 15 mTorr at 100 °C for 30 h.

DOI: 10.1021/ja512383b
J. Am. Chem. Soc. 2015, 137, 2658−2664

TGA, SEM, ICP, and IR. TGA data were collected on a PerkinElmer TGA 7 system under flowing N_2. Scanning electron microscopy (SEM) was carried out with a JEOL JSM-5610 microscope. The molar ratios of Na, Mn, and Fe were measured by ICP analysis. For ICP measurements, the samples were heated under air at 500 °C for 6 h and then were dissolved in concentrated HNO_3 and HCl (1:2 v/v) in a polypropylene bottle. Fourier transformation infrared (FT-IR) spectroscopy data was collected at room temperature on a Thermo Scientific Nicolet iS5 FT-IR Spectrometer with an iD5 ATR Accessory. The powder samples were simply loaded on the diamond crystal without any further protection. The collection time was 1 min.

XRD and Synchrotron and Neutron Diffraction. XRD patterns were collected on a Rigaku R-Axis Spider diffractometer with an image-plate detector, a graphite monochromator, and Cu Ka radiation (λ = 1.5418 Å). All powder samples were sealed in 0.3 mm glass capillaries in an Ar-filled glovebox. High-resolution synchrotron XRD data of $Na_{2-\delta}$MnHCF were collected at the X 14A beamline of the National Synchrotron Light Source at Brookhaven National Laboratory with a 1D linear-position-sensitive silicon-strip detector with 640 channels at a distance of 1433 mm and an X-ray wavelength of about 0.78 Å. The diffraction pattern was collected between 6 and 60°, with a 2° step and a duration time of 30 s/step. TOF powder neutron diffraction data were collected on the NOMAD beamline at 300 K at the Spallation Neutron Source (SNS) of Oak Ridge National Laboratory. About 250 mg of a powder sample was packed into a 3 mm diameter quartz capillary. A data collection time of 120 min was used. The details of solving and refining the structures of the R and M phases are presented in the Supporting Information.

Electrochemical Measurement. Electrochemical performances were evaluated with CR2032 coin half-cells composed of a cathode and a metallic-sodium anode with 1 mol L^{-1} $NaClO_4$ in 1:1 diethyl carbonate/ethylene carbonate electrolyte containing 10 wt % fluoroethylene carbonate and a Whatman glass-fiber separator. The cathodes were prepared by mixing 70 wt % active material with 20 wt % Ketjen black and 10 wt % polytetrafluoroethylene (PTFE) binder; the mixture was rolled into thin sheets and punched into circular electrodes 0.8 cm in diameter. The typical electrode mass was 3−5 mg. In preparation of full cells, an anode of 95% Kureha hard carbon and 5% sodium carboxymethyl cellulose/styrene−butadiene rubber (CMC/SBR) binder was used. All coin cells were assembled in an Ar-filled glovebox. The cells were galvanostatically cycled under different current densities at room temperature between 2.0 and 4.0 V versus Na^+/Na.

Ex situ XRD. For ex situ XRD measurements, the cells were charged and discharged at a low current of 5 mA g^{-1} to a certain voltage and then were disassembled in the glovebox. After being rinsed in dimethyl carbonate, the electrodes were sealed in 0.3 mm diameter capillaries. Ex situ XRD patterns were collected on Rigaku R-Axis Spider diffractometer.

■ ASSOCIATED CONTENT

Supporting Information

Details of methods to solve and refine the structure of R-$Na_{2-\delta}$MnHCF and M-$Na_{2-\delta}$MnHCF; SEM image; refinement results of XRD pattern and TOF neutron-diffraction pattern of R-$Na_{2-\delta}$MnHCF; charge and discharge curves of M-$Na_{2-\delta}$MnHCF on the 1st, 2nd, 5th, and 10th cycles; rate performance of a hard carbon−R-$Na_{2-\delta}$MnHCF full cell; Comparison of reported cathode materials for sodium-ion batteries. This material is available free of charge via the Internet at http://pubs.acs.org.

■ AUTHOR INFORMATION

Corresponding Author

*jgoodenough@mail.utexas.edu

Author Contributions

J.S., L.W., and Y.L. contributed equally to this work.

Notes

The authors declare no competing financial interest.

■ ACKNOWLEDGMENTS

This work was supported by the Advanced Research Projects Agency-Energy, United States Department of Energy, under contract DE-AR0000297. The work at Stony Brook University and Brookhaven National Laboratory was supported by the United States Department of Energy, the Assistant Secretary for Energy Efficiency and Renewable Energy, Office of Vehicle Technologies under contract nos. DE-AC02-98CH10886 and DE-SC0012704. Use of the National Synchrotron Light Source, Brookhaven National Laboratory, was supported by the United States Department of Energy, Office of Science, Office of Basic Energy Sciences, under contract nos. DE-AC02-98CH10886 and DE-SC0012704. Research conducted at ORNL's Spallation Neutron Source was sponsored by the Scientific User Facilities Division, Office of Basic Energy Sciences, United States Department of Energy.

■ REFERENCES

(1) Yang, Z. G.; Zhang, J. L.; Kintner-Meyer, M. C. W.; Lu, X. C.; Choi, D. W.; Lemmon, J. P.; Liu, J. *Chem. Rev.* **2011**, *111*, 3577−3613.

(2) Pan, H. L.; Hu, Y. S.; Chen, L. Q. *Energy Environ. Sci.* **2013**, *6*, 2338−2360.

(3) Palomares, V.; Serras, P.; Villaluenga, I.; Hueso, K. B.; Carretero-Gonzalez, J.; Rojo, T. *Energy Environ. Sci.* **2012**, *5*, 5884−5901.

(4) Kim, S. W.; Seo, D. H.; Ma, X. H.; Ceder, G.; Kang, K. *Adv. Energy Mater.* **2012**, *2*, 710−721.

(5) Wessells, C. D.; Huggins, R. A.; Cui, Y. *Nat. Commun.* **2011**, *2*, 550.

(6) Pasta, M.; Wessells, C. D.; Huggins, R. A.; Cui, Y. *Nat. Commun.* **2012**, *3*, 1149.

(7) Wu, X.; Cao, Y.; Ai, X.; Qian, J.; Yang, H. *Electrochem. Commun.* **2013**, *31*, 145−148.

(8) Kim, D. J.; Jung, Y. H.; Bharathi, K. K.; Je, S. H.; Kim, D. K.; Coskun, A.; Choi, J. W. *Adv. Energy Mater.* **2014**, *4*, 1400133.

(9) Asakura, D.; Li, C. H.; Mizuno, Y.; Okubo, M.; Zhou, H. S.; Talham, D. R. *J. Am. Chem. Soc.* **2013**, *135*, 2793−2799.

(10) Lu, Y. H.; Wang, L.; Cheng, J. G.; Goodenough, J. B. *Chem. Commun.* **2012**, *48*, 6544−6546.

(11) Wang, L.; Lu, Y. H.; Liu, J.; Xu, M. W.; Cheng, J. G.; Zhang, D. W.; Goodenough, J. B. *Angew. Chem., Int. Ed.* **2013**, *52*, 1964−1967.

(12) Wu, X.; Deng, W.; Qian, J.; Cao, Y.; Ai, X.; Yang, H. *J. Mater. Chem. A* **2013**, *1*, 10130−10134.

(13) You, Y.; Wu, X.-L.; Yin, Y.-X.; Guo, Y.-G. *Energy Environ. Sci.* **2014**, *7*, 1643−1647.

(14) Yue, Y. F.; Binder, A. J.; Guo, B. K.; Zhang, Z. Y.; Qiao, Z. A.; Tian, C. C.; Dai, S. *Angew. Chem., Int. Ed.* **2014**, *53*, 3134−3137.

(15) Herren, F.; Fischer, P.; Ludi, A.; Halg, W. *Inorg. Chem.* **1980**, *19*, 956−959.

(16) Kareis, C. M.; Lapidus, S. H.; Her, J. H.; Stephens, P. W.; Miller, J. S. *J. Am. Chem. Soc.* **2012**, *134*, 2246−2254.

(17) Imanishi, N.; Morikawa, T.; Kondo, J.; Takeda, Y.; Yamamoto, O.; Kinugasa, N.; Yamagishi, T. *J. Power Sources* **1999**, *79*, 215−219.

DOI: 10.1021/ja512383b
J. Am. Chem. Soc. 2015, 137, 2658−2664

(18) Ganguli, S.; Bhattacharya, M. *J. Chem. Soc., Faraday Trans. 1* **1983**, *79*, 1513−1522.
(19) Kulesza, P. J.; Malik, M. A.; Denca, A.; Strojek, J. *Anal. Chem.* **1996**, *68*, 2442−2446.
(20) Her, J. H.; Stephens, P. W.; Kareis, C. M.; Moore, J. G.; Min, K. S.; Park, J. W.; Bali, G.; Kennon, B. S.; Miller, J. S. *Inorg. Chem.* **2010**, *49*, 1524−1534.
(21) Xiao, P.; Song, J.; Wang, L.; Goodenough, J. B.; Henkelman, G. Manuscript in preparation.

DOI: 10.1021/ja512383b
J. Am. Chem. Soc. 2015, 137, 2658−2664